

LA-UR-15-28232 (Accepted Manuscript)

“Trunk-like” heavy ion structures observed by the Van Allen Probes

Zhang, J. C.; Kistler, L. M.; Spence, H. E.; Wolf, R. A.; Reeves, Geoffrey D.; Skoug, Ruth M.; Funsten, Herbert O.; Larsen, Brian Arthur; Niehof, J. T.; MacDonald, E. A.; Friedel, Reinhard Hans Walter; Ferradas, C. P.; Lou, H.

Provided by the author(s) and the Los Alamos National Laboratory (2016-12-02).

To be published in: Journal of Geophysical Research: Space Physics

DOI to publisher's version: 10.1002/2015JA021822

Permalink to record: <http://permalink.lanl.gov/object/view?what=info:lanl-repo/lareport/LA-UR-15-28232>

Disclaimer:

Approved for public release. Los Alamos National Laboratory, an affirmative action/equal opportunity employer, is operated by the Los Alamos National Security, LLC for the National Nuclear Security Administration of the U.S. Department of Energy under contract DE-AC52-06NA25396. Los Alamos National Laboratory strongly supports academic freedom and a researcher's right to publish; as an institution, however, the Laboratory does not endorse the viewpoint of a publication or guarantee its technical correctness.

“Trunk-like” heavy ion structures observed by the Van Allen Probes

J.-C. Zhang¹, L. M. Kistler¹, H. E. Spence¹, R. A. Wolf², G. Reeves³, R. Skoug³, H. Funsten³, B. A. Larsen³, J. T. Niehof¹, E. A. MacDonald⁴, R. Friedel³, C. P. Ferradas¹, and H. Luo⁵

¹Space Science Center, University of New Hampshire, Durham, NH 03824, USA

²Department of Physics and Astronomy, Rice University, Houston, TX 77005, USA

³ISR Space Science and Applications, Los Alamos National Laboratory, Los Alamos, NM 87545, USA

⁴Geospace Physics Laboratory, NASA/GSFC, Greenbelt, MD 20771, USA

⁵Institute of Geology and Geophysics, Chinese Academy of Sciences, Beijing 100029, P. R. China

To be re-submitted to *Journal of Geophysical Research – Space Physics*

Mailing address of the corresponding author¹:

8 College Road, Morse Hall, SSC, Durham, NH 03824, USA

Key Points:

1. A new type of ion spectral structure – “trunk-like” – is reported
2. The trunk structures are present in He⁺ and O⁺ ions but not in H⁺
3. Simulations are performed to gain insight into the trunk formation mechanism

Keywords:

Ion structure, ion injection, inner magnetosphere, magnetic storm, magnetic cloud, Van

Allen Probes

Abstract. Dynamic ion spectral features in the inner magnetosphere are the observational signatures of ion acceleration, transport, and loss in the global magnetosphere. We report “trunk-like” ion structures observed by the Van Allen Probes on 2 November 2012. This new type of ion structure looks like an elephant’s trunk on an energy-time spectrogram, with the energy of the peak flux decreasing Earthward. The trunks are present in He^+ and O^+ ions but not in H^+ . During the event, ion energies in the He^+ trunk, located at $L = 3.6$ – 2.6 , $\text{MLT} = 9.1$ – 10.5 , and $\text{MLAT} = -2.4$ – 0.09° , vary monotonically from 3.5 to 0.04 keV. The values at the two end points of the O^+ trunk are: energy = 4.5–0.7 keV, $L = 3.6$ – 2.5 , $\text{MLT} = 9.1$ – 10.7 , and $\text{MLAT} = -2.4$ – 0.4° . Results from backward ion drift path tracings indicate that the trunks are likely due to 1) a gap in the nightside ion source or 2) greatly enhanced impulsive electric fields associated with elevated geomagnetic activity. Different ion loss lifetimes cause the trunks to differ among ion species.

AGU Index Terms:

2740 [Primary] Magnetospheric configuration and dynamics

2760 Plasma convection (2463)

2764 Plasma sheet

2778 Ring current

2768 Plasmasphere

Running Title: ZHANG ET AL.: Trunk Ion Structures

1. Introduction

Particles that originate in the solar wind or ionosphere are injected from the plasma sheet freshly into the inner magnetosphere during magnetic storms and substorms. The injection of the particles into the inner magnetosphere results in a toroid-shaped ring current at radial distances of $\sim 2-7 R_E$. The current is carried primarily by $\sim 1-200$ keV ions (mainly H^+ , O^+ , and He^+) and electrons, which azimuthally drift around the Earth [Gonzalez *et al.*, 1994; Daglis *et al.*, 1999]. Particles in the ring current are lost via dayside flow out the magnetopause, as well as by charge exchange, Coulomb collisions, and wave-particle interactions [e.g., Kistler *et al.*, 1989; Fok *et al.*, 1991; Jordanova *et al.*, 1996; Kozyra *et al.*, 1998; Liemohn *et al.*, 1999; Liemohn *et al.*, 2001].

The inner magnetosphere is a highly dynamic region where multiple populations, including the cold plasmasphere, energetic ring current, and relativistic radiation belt particles, overlap and interact with each other. The dynamics of these particle populations are controlled by the time-varying magnetic and electric fields in this region. Conversely, the particle populations also generate currents that affect both the magnetic field and the electric field [Gonzalez *et al.*, 1994; Daglis *et al.*, 1999].

Several spacecraft missions have detected various ion spectral features in the inner magnetosphere. These include “nose-like” structures [e.g., Smith and Hoffman, 1974; Ejiri *et al.*, 1980; Shirai *et al.*, 1997; Fennell *et al.*, 1998; Peterson *et al.*, 1998; Li *et al.*, 2000; Ganushkina *et al.*, 2001; Buzulukova *et al.*, 2003; Ebihara *et al.*, 2004; Vallat *et al.*, 2007], “wedge-like” dispersions [e.g., Ebihara *et al.*, 2001; Yamauchi *et al.*, 2006], ion gaps [e.g., Kovrazhkin *et al.*, 1999], and stagnation dips [e.g., Lennartsson *et al.*, 1979]. These ion structures are named after the characteristic shapes of energy bands or gaps in the energy-time spectrograms of *in situ* measured ion fluxes. They constitute

78 the observational signatures of ion acceleration, transport, and loss in the global
79 magnetosphere. The ion structures are attributed to the single or combined effect of
80 several factors governing ion access to the inner magnetosphere: convection, corotation,
81 magnetic gradient and curvature drifts, ion losses, and changes in the convection electric
82 field and/or the ion source population. In the inner magnetosphere, keV ions are
83 characterized by more complex spectral structures than electrons. The main reason is that
84 the directions of the corotation and magnetic gradient/curvature drift are opposite for ions
85 but the same for electrons. Near the inner boundary of the plasma sheet where the
86 corotation electric field becomes more important than the large-scale dawn-to-dusk
87 convection electric field, a net ion drift direction can be either eastward or westward, but
88 electrons normally drift eastward.

89 In this study, we report a new type of ion structure observed by the Helium,
90 Oxygen, Proton, and Electron (HOPE) mass spectrometer in the Radiation Belt Storm
91 Probes - Energetic Particle Composition and Thermal Plasma (RBSP-ECT) suite onboard
92 the Van Allen Probes. The spectral feature of the new ion structures is similar to an
93 elephant's nose, i.e., "trunk-like". This paper is organized as follows: after the
94 introduction (current section), we describe the instrumentation of the Van Allen Probes in
95 Section 2. Section 3 presents the observations of the trunk-like ion structures, solar wind
96 and geomagnetic conditions, and trunk simulations. Discussion and conclusions from the
97 work follow in Section 4.

98

99 2. Instrumentation

100 The Van Allen Probes mission, formerly known as the Radiation Belt Storm
101 Probes (RBSP) mission [Kessel *et al.*, 2013; Mauk *et al.*, 2013], consists of two
102 spacecraft in almost the same highly-elliptical, low-inclination (10°) orbit with a perigee
103 of 1.1 Earth radii (R_E), an apogee of $5.8 R_E$, and a period of ~ 9 hours. The perigee-apogee
104 line, i.e., the line of apsides, precesses in local time at a rate of $\sim 210^\circ$ per year. The orbits
105 of the two probes are slightly different and one probe laps the other every ~ 2.5 months.
106 As a result, the inter-spacecraft distance periodically varies between ~ 0.1 to $\sim 5 R_E$ and
107 resampling times for a specific region change from minutes to 4.5 hours. A
108 comprehensive suite of instruments, identical on the two Van Allen Probes (-A and -B),
109 measures a variety of parameters in particles (electrons, ions, and ion composition),
110 magnetic field (\mathbf{B}), electric field (\mathbf{E}), and waves ($\delta\mathbf{E}$ and $\delta\mathbf{B}$).

111 HOPE [Funsten *et al.*, 2013] is the low-energy instrument of the RBSP-ECT
112 instrument suite [Spence *et al.*, 2013]. Using an electrostatic top-hat analyzer and the
113 time-of-flight technology, the HOPE mass spectrometer measures electrons and ions in
114 the energy range of ~ 1 eV–52 keV and distinguishes composition of three major ion
115 species, H^+ , He^+ , and O^+ . The measurement methodology and design of the HOPE
116 instrument are intended for the reduction of the intense radiation background induced by
117 relativistic particles and for valid plasma measurements in the harsh environment of the
118 Earth’s radiation belts.

119

3. Observations and Simulations

3.1. Trunk-like Ion Structures

Figure 1 shows H^+ , He^+ , and O^+ energy-time flux spectrograms from HOPE on the Van Allen Probe-A for a full 9-hour orbit from 1320 to 2220 UT on 2 November 2012. HOPE data presented here are spin-averaged from Release 2 of the ECT data set. For the purpose of comparison, the fluxes of different ion species are plotted in the same range. Several ephemeris parameters of the spacecraft are included at the bottom of the figure. The L value ($=L_{TS04}$) is computed with the Tsyganenko and Sitnov empirical magnetic field model (TS04) [Tsyganenko and Sitnov, 2005]. While the inclination of the spacecraft orbit is fixed at 10° , its magnetic latitude (MLAT) can vary in the range of -21° to 21° due to the tilt of the geomagnetic axis and the precession of the line of apsides [Mauk et al., 2013]. The plotting period is centered at perigee and extends for an entire orbit, i.e., 8.98 hours. The perigee, marked by the vertical red dashed line, is at the time when the radial distance (DIST) is the minimum.

While nose-like and wedge-like spectral features are present in the spectrogram plots of all the three ion species, trunk-like structures are clearly displayed only in those of heavy He^+ and O^+ ions on the inbound perigee pass. HOPE electron spectra (not shown) do not exhibit trunk features. The He^+ trunk (Figure 1b) extends to a much lower energy than the O^+ trunk (Figure 1c), i.e., to 43 eV in He^+ compared to 723 eV in O^+ . At higher and lower energy compared to the base of the trunks, nose-like spectral features are present; the lower-energy feature is more like a secondary trunk (also see Figure 2b). These trunk structures differ from the well-known nose structures. Noses are observed at a single energy across a range of L; the energy of the peak flux within a trunk shows a

strong dependence on L. Table 1 lists several properties of the main He^+ trunk and the O^+ trunk as shown in Figures 1b and 1c. The six columns show the values of UT, He^+ energy, O^+ energy, L, MLT, and MLAT at several sample points along the central line of the trunk structures, respectively. The first and fourth rows indicate the values at the two end points of the He^+ trunk (Figure 1b): energy = 3.5–0.04 keV, L = 3.6–2.6, MLT = 9.1–10.5, and MLAT = -2.4–0.09°. The values at the two end points of the O^+ trunk (Figure 1c) shown in the first and fifth rows are: energy = 4.5–0.7 keV, L = 3.6–2.5, MLT = 9.1–10.7, and MLAT = -2.4–0.4°.

No trunk-like structure exists on the outbound perigee pass. The inner edge of lower L-shell access in each species, i.e., the lowest penetration boundary of convecting ions, is deeper than that on the inbound pass. The difference in the lowest injection L-value between the inbound and outbound passes is 0.6 (0.8) for H^+ (He^+ and O^+). This is due to the dependence of the location of the inner injection boundary on MLT [Ejiri *et al.*, 1980].

Figure 2 illustrates He^+ spectral features observed by the HOPE instrument on three consecutive orbits of the Van Allen Probe-B (a, b, and d) and one orbit of the Van Allen Probe-A (c). Figure 2c is the same as Figure 1b. He^+ spectrograms before and after the trunk orbit of the Van Allen Probe-A (Figure 2c) are not shown because they are almost identical to their counterparts on the Van Allen Probe-B (Figures 2a and 2d). The spectrograms of He^+ , as well as those of H^+ and O^+ (not shown), from the two spacecraft in the same orbit with a temporal separation of 50 minutes are comparable. The trunk on the Van Allen Probe-A has a slightly wider spatial extent than that on the Van Allen Probe-B. Trunk structures were not detected on the inbound passes of the orbits right

before and after the trunk orbit (Figures 2a and 2d). As for the outbound passes of the four orbits (Figures 2a-d), no trunk is present at all, but in Figure 2d a broad-energy band appears on the outbound pass over the energy range of the trunk and extends to a low L-shell, where $L = 2.3$, $MLT=1.0$, and $MLAT = 9.8^\circ$.

3.2. Solar Wind and Geomagnetic Conditions

Figure 3 shows 1-minute solar wind plasma number density N , bulk flow speed V , dynamic pressure P_{dyn} , IMF B_y and B_z in the GSM coordinates, polar cap potential drop (PCP), K_p , and the $Sym-H$ index during the moderate storm occurring from 31 October to 3 November 2012. The high-resolution solar wind measurements are from the online OMNIWeb Plus dataset [Papitashvili and King, 2006]. There is an ~8-hr gap in the solar wind data close to the end of the plotting period. PCP, a proxy for the convection electric field intensity, is given by $PCP = 57.6 P_{dyn}^{1/3} E / (P_{dyn}^{1/2} + 0.43E) + 10^{-4} V^2$, where PCP is in kV, P_{dyn} in nPa, solar wind electric field E in mV/m, and V in km/s. $E = 0$ for northward IMF and $V|B_z|$ for southward. The first term in the PCP formula is given by Siscoe *et al.* [2002] and the second is a viscous term from Boyle *et al.* [1997]. The solar wind and PCP data are shifted backward by 10 minutes to align the solar wind shock with the storm sudden commencement (SSC) at 1540 UT, 31 October 2012. The 10-minute time shift is within expected aberrations when solar wind data are propagated from a satellite (e.g., around the first Lagrange point L1) to the Earth for the creation of the OMNIWeb database [Weimer *et al.*, 2003; Weimer and King, 2008]. The first vertical red dashed line marks the arrival time of the solar wind shock. The two vertical magenta dot-dashed (dotted) lines indicate the time period of the trunk observed by the Van Allen

Probe-B (A), i.e., 1537:20 – 1612:20 (1627:20 – 1700:40) UT, 2 November 2012. In Figures 3d and 3g, the horizontal black dashed line marks the zero value.

The moderate storm, during which minimum $Sym-H$ is equal to -68 nT at 2001 UT on 1 November 2012, was driven by a magnetic cloud (MC) with an extended sheath region [Burlaga *et al.*, 1981; Zhang *et al.*, 2004]. The three vertical red dashed lines in Figure 3 denote both of the sheath and MC regions. Further solar wind disturbances behind the MC event may be due to the eroded MC flux rope, which results from magnetic reconnection at the boundary between the sheath and MC [Ruffenach *et al.*, 2012]. The trunks occurred in the middle recovery phase of the geomagnetic storm.

3.3. Backward Ion Drift Path Tracings

Figure 4 demonstrates total drift time results from the backward tracings of ion drift trajectories from given probe positions for 50 hours or until the ions reach the assumed tailward injection boundary at $L=10$. Tracing results under different conditions (see below) are presented. The particle tracing technique has been previously utilized [e.g., Buzulukova *et al.*, 2002; Ebihara *et al.*, 2008]. The tracing simulations are performed with the Weimer96 convection electric field [Weimer, 1996], a corotational electric field, and a dipole magnetic field. Charge exchange is assumed to be the only ion loss process along the drift paths. For the charge exchange loss calculations, equatorial neutral hydrogen number density is inferred from a model derived by [Hodges, 1994] and charge exchange cross sections are given by [Smith and Bewtra, 1978a].

Figures 4a and 4b show the drift time from $L=10$ to the observation location with the specified time-dependent electric fields using the standard Weimer96 settings. Only the color bars are different between the nominal tracing results (Figures 4a and 4b). This

is to emphasize the difference in the drift time in the isolated low energy region, the “island”, in Figure 4b. If a trajectory never reaches $L=10$ in the 50 tracing hours, meaning that either the drift path is closed or the particle drifts very slowly, then white is shown. As can be seen, with a steady tail source, an island structure is formed and has an outer boundary featuring a trunk-like shape at the lower L end. Therefore, one way that the trunk could be formed (Case #1) is with a time-dependent variation in the source, where the injection of ions in the island with shorter drift time (≤ 34.0 hrs) than trunk ions is halted. The resulting drift time spectrum, computed assuming no source population if the total drift time is in the range of 29.2–34.0 hrs, is shown in Figure 4c. The choice of the temporal gap in the source is roughly determined by the realism of the observed trunk spectral features shown in Figure 1b, especially the trunk thickness. This threshold would depend on the specifics of a particular event.

The disappearance of the ions in the island spans ~ 5 hrs in UT. It would rotate eastward (see the green line in Figure 6a) and form a cold-ion gap along the drift path, i.e., for several hours in MLT. This localized structure might be the reason that the trunk was not detected by the Van Allen Probe-B at the same MLT location during the next orbit (Figure 2d), and there was a disappearance of cold ions ($< \sim 200$ eV) on the outbound pass of the Van Allen Probe-B at ~ 2 MLT from 0240-0350 UT on 3 November 2012 (Figure 2d).

The effect of a second mechanism to form the trunk (Case #2) is shown in Figure 4d. In this case, a modified solar wind condition (i.e., Weimer96 input IMF B_z is subtracted by 40 nT from 0900 to 2200 UT on 1 Nov. 2012) is simulated. Surprisingly, particle tracing within these fields directly yields a trunk (the low L side of the arch structure) in the accessibility to particles from the presumed $L=10$ injection region. The

peak value and duration of the made-up southward IMF B_z are too “extreme” to exist in reality. This tracing run is for the purpose of experiment. Still, the modification to IMF B_z aims to create a cumulative effect on ion drift of greatly enhanced impulsive electric fields associated with elevated geomagnetic activity, which are lacking in the empirical Weimer96 model. A set of peak values and durations of IMF B_z have been tested. It turns out that a “decent” arch structure (Figure 4d) can be created with the input modification above.

Note that the observed He^+ trunk (Figure 1b) and the simulated trunks (Figures 4c and 4d) differ in several aspects, e.g., in ion energy and occurrence UT. The separate “island”, which is formed in the simulations with the standard Weimer96 (Figure 4b), is not evident in the observations. The reason for the island, and why it might not be observed in this case, is discussed below. The observations show that the trunk feature connects smoothly to structures in the ion spectra. For example, in Figures 1b and 1c, there is a peak in the H^+ and O^+ (clearer) fluxes at around 4 keV near 1600 UT, which is blended with the observed trunk feature. However, the simulated trunks are not connected to other spectral structures at all; this simulation result yet implies that the trunk ion populations are different from the non-trunk populations (difficult to be identified in the observations, though). The data-model discrepancies may be due to the fact that the empirical Weimer96 electric field model, combined with the simple dipole magnetic field model, cannot accurately reproduce particular ion spectral features, but can still indicate the trends. While being able to fairly well reproduce the large-scale dawn-to-dusk convection electric field, Weimer96 does not include impulsive, localized electric fields associated with substorm injections [e.g., *Zhang et al.*, 2008; *Zhang et al.*, 2009]. The small-scale electric fields can cause diffusion, which may be effective enough to make

the spectral structures blur into each other [Gkioulidou *et al.*, 2014; Yang *et al.*, 2014]. In addition, we only consider the ion source region from the outer boundary (assumed at $L = 10$) and do not include any other ion source or pre-existing particles in the trunk region. This can also result in much simpler or more idealized spectral features in the simulation results than those in the observations.

Wedges are not reproduced at all, because no variation is applied to the distribution function of the tailward ion source [Ebihara *et al.*, 2001]. Noses are reasonably well reproduced with Weimer96 and the dipole magnetic field. The fine spectral features in noses, i.e., multiple horizontal gaps in the higher-energy ions, are associated with the variations in solar wind (see Figure 3). Another run with constant inputs to Weimer96 is performed to evaluate the effects of the solar wind variations. The model inputs include Earth’s dipole tilt angle, solar wind N and V , and IMF B_y and B_z [Weimer, 1996]. The fixed input values are those at 0600 UT, 31 Oct. 2012, i.e., the plot start time of Figure 3. As shown in Figure 4e, when inputs to Weimer96 are fixed, only one main nose is present. The nose is basically formed with more deeply injected ions when the magnitudes of their $\mathbf{E} \times \mathbf{B}$ drift and magnetic gradient/curvature drift are comparable. The “cancelled” net ion drift (due to the opposite directions of the two types of drifts) allows those ions to move more inward instead of around the Earth in either the eastward or westward direction. The variations in the solar wind parameters, affecting ion drift magnitudes, change the energy of those nose ions and thus result in the multiple spectral bands in the nose energy range [Buzulukova and Vovchenko, 2008].

Figure 5 shows the fraction of the initial flux remaining (f/f_0) after charge exchange losses along the drift path for the species H^+ , He^+ , and O^+ , computed with the same halted ion source as in Figure 4c. Because the charge exchange loss rates depend on

the ion species and energy, and how deeply the trajectory penetrates in L-value [Smith and Bewtra, 1978b], these losses can create spectral gaps and features that appear differently for different species. There are clearly different depletion levels among H^+ , He^+ , and O^+ . The differences are more distinct at lower L-shells and in higher energies. Since H^+ has the shortest charge exchange lifetime, $H^+ f/f_0$ in the upper energy trunk is almost 0, while He^+ is barely depleted. Thus the species dependence observed is consistent with the model that the trunk is caused by ions on drift paths with long drift time. The pitch angle distribution of trunk ions is centered around 90° (not shown), which is also consistent with the effect of charge exchange on drifting particles, i.e., becoming more anisotropic over time [Goldstein et al., 2012]. Coulomb collisions with cold plasma in the plasmasphere [Fok et al., 1991] are perhaps the other loss process that could further deplete ions and even wipe out H^+ and O^+ in the lower energy trunk as shown in Figure 1. For the trunk energy range, H^+ still has the shortest Coulomb collision lifetime among the three ion species [Fok et al., 1991].

Figure 6 shows 50-hour backward tracing of drift paths for three singly-charged ions with energies of 0.1, 0.5, and 10 keV (see the horizontal dotted lines in Figure 4) at 1635 UT for the cases indicated in Figures 4b (left panel: Case #1), the Weimer96 electric field, and 4d (right panel: Case #2), the “extreme” electric field. The 0.5 keV ion trajectory corresponds to the trunk. The ion trajectories either last for 50 hrs or end at $L \sim 10$ when the ions reach the boundary. The 10.0 keV ion drifts very slowly on a closed drift path in Case #1, but it is on an open drift path and has access to the tailward ion source in Case #2. Before reaching $L=10$, the 0.5 keV trunk ion drifts an extra circle around the Earth in both cases. The 0.1 keV ion has a similar trajectory to the 0.5 keV ion in Case #1, but it is trapped on a closed drift trajectory in Case #2. More ion tracings

indicate that all the trunk ions are from a source region with a narrow MLT range. For example, the ion source at L=10 for the trunk ions in Figure 4c is in the MLT range of 21.6-22.8. In addition, in Case #1, a majority of the trunk ions have total drift time just over 34.0 hrs. They were injected at L=10 at ~0600 UT on 1 Nov. 2012, which is in the middle of the storm main phase. If the injection of those ions under the trunk arch which have total drift time from 29.2 to 34.0 hrs and MLT at L=10 from 22.2 to 22.9 (e.g., the green line in Figure 6a) is halted, a trunk would be formed from Figure 4b, as shown in Figure 4c. It is not expected to suspend the ion source for almost 5 hours in UT during the main phase of the moderate storm. However, the source suspension is required only in low energies (i.e., $< \sim 800$ eV in the trunk region), and the total drift time of the suspended ions seems to dominate a shorter time range (i.e., ~ 30 – 31 hrs), as shown in Figure 4b. In reality, the temporal gap of the ion source could be much narrower. The cause of the source gap might be associated with a variation in the cold ion source [e.g., *Ebihara et al.*, 2001] or the activity of a “depleted channel” or “plasma bubble” during the storm, which is characteristic of Earthward-traveling low-entropy flux tubes [e.g., *Sergeev and Lennartsson*, 1988; *Zhang et al.*, 2008; *Zhang et al.*, 2009].

Another figure, Figure 7, is intended to highlight the drift path differences between ions inside and outside the island (Figures 4a and 4b). The particle tracing setup for Figure 7 is the same as Figure 6a, but for 0.5 and 2.0 keV singly-charged ions at 1600 UT, 2 November 2012. The backward-traced ions start from the spacecraft location at the time, i.e., from L = 4.2 and MLT = 8.4. At the time point, the particle energies are just below and above the spectral gap that separates the island from its surrounding spectral features. Consistent with the results in Figure 6a, the island ion (0.5 keV) drifts around the Earth almost a full circle more than the non-island ion (2.0 keV). The spectral gap

(Figures 4a and 4b) is thus caused by the distinct differences in the drift time and paths between the island and non-island ions. Note that the 2.0 keV ion in Figure 7 drifts eastward but the 10.0 keV ion in Figure 6a goes westward. The reason is that their dominant drift component is different, i.e., $\mathbf{E} \times \mathbf{B}$ drift for the former but gradient-curvature drift for the latter.

4. Discussion and Conclusions

We report a new type of ion spectral feature in the inner magnetosphere – trunk-like ion structure. The trunk structures, observed *in situ* by the RBSP-ECT HOPE instrument onboard the two Van Allen Probes on 2 November 2012, are present in the spectrograms of He^+ and O^+ ions but not in those of H^+ . For the particular event, ion energies in the He^+ trunk, which is located at $L = 3.6\text{--}2.6$, $\text{MLT} = 9.1\text{--}10.5$, and $\text{MLAT} = -2.4\text{--}0.09^\circ$, vary monotonically from 3.5 to 0.04 keV. The values at the two end points of the O^+ trunk are: energy = 4.5–0.7 keV, $L = 3.6\text{--}2.5$, $\text{MLT} = 9.1\text{--}10.7$, and $\text{MLAT} = -2.4\text{--}0.4^\circ$. Possible reasons that the trunk has been observed by the Van Allen Probes and not by earlier space missions, such as Cluster and THEMIS, include 1) more frequent crossings of the inner edge of the plasma sheet, and 2) higher-fidelity measurements of plasma-sheet ion fluxes and composition by the HOPE instrument in the harsh radiation belt environment.

The trunk-like structures are different from previously reported nose-like and wedge-like ion structures, and require a new formation mechanism. Noses are characterized by narrow bands in energy, which extend down to low L-shells but are nearly constant in energy [e.g., *Smith and Hoffman*, 1974; *Ejiri*, 1978]. They are normally

356 due to the deeper injection of ions with a specific energy when the westward and
 357 eastward components of the $\mathbf{E} \times \mathbf{B}$ and gradient-curvature drifts of the ions become
 358 comparable in magnitude. *Ebihara et al.* [2001] suggested that a wedge-like structure,
 359 containing sub-keV ions, should result from the energy-dependent Earthward drift of ions
 360 in the plasma sheet when the distribution function of the ion source changes in time and
 361 space. The ion source variation can be related to a substorm injection and/or an ion flow
 362 channel in the tail. Although the outer layer of a wedge [e.g., *Ebihara et al.*, 2001;
 363 *Yamauchi et al.*, 2006; *Ebihara et al.*, 2008] looks similar to a trunk structure, the change
 364 of the structure thickness in energy and L is opposite between a trunk and a wedge: the
 365 higher the ion energy or the L, the wider the trunk but the thinner the wedge. The time
 366 scale of an observed wedge is also much smaller than a trunk, typically ~ 10 versus ~ 30
 367 minutes on the Van Allen Probes. While noses and wedges often display multiple ion
 368 energy bands, the trunks we have reported only exist as a single, narrow structure on the
 369 inner ion penetration boundary. Another distinct difference between trunks and other ion
 370 structures is in occurrence frequency. Noses and wedges (predominantly on the dayside
 371 [*Ebihara et al.*, 2001]) occur frequently close to the inner edge of the plasma sheet.
 372 However, the trunks apparently occur only rarely. Visual inspection of HOPE ion spectra
 373 for ~ 2 months, i.e., 26 October 2012 – 31 December 2012, reveals only two more well-
 374 structured trunk structures in both He^+ and O^+ on each probe on 4 and 14 November,
 375 respectively. The two clear trunk events were also observed in the morning sector with an
 376 MLT range of ~ 8 – 10 . Moreover, they occurred in the recovery phase of a magnetic storm
 377 as well. The former occurred in the late recovery phase of the 1 November 2012
 378 moderate storm and the latter was present in the middle recover phase of an intense storm
 379 (min. $\text{Sym-H} = -117$ nT at 0725 UT on 14 November 2012). Collecting and examining

more trunks to obtain their occurrence frequency, location, and conditions will be a topic for future work.

To gain insight into how trunks are formed, we perform backward tracings of ion drift paths from one-whole-orbit probe positions to the ion source region ($L=10$) while considering the effect of the charge exchange loss. While there are several puzzling features in the trunks, the most significant one is their relative spectral narrowness. Our tracing results show that the source location for the trunk ions is small and the particles are initially injected over a short time. These most likely account for the narrowness of the trunk feature. The trunk ions are also found to have prolonged total drift time from $L=10$ to the observation location, circling the Earth an extra time before reaching the observation points. The drift time is long enough to allow charge exchange and Coulomb collisions to take effect and cause the trunk-feature differences among ion species due to their different loss lifetimes. In particular, because H^+ has the shortest lifetime, it is completely depleted by the time it arrives at the region where a trunk would form. As a result, the trunks are present only in heavy ions. It is indicated that a trunk can be formed in two possible ways: 1) a gap in the nightside ion source or 2) greatly enhanced impulsive electric fields associated with elevated geomagnetic activity. Similar variation in the distribution function of the ion source has been used to explain the spectral gaps between wedges [Ebihara *et al.*, 2001]. However, an experimental run with the made-up solar wind condition implies that a trunk may also be formed from large impulsive electric fields that are often present during substorms/storms [Zhang *et al.*, 2008; Zhang *et al.*, 2009]. Further investigation is required to evaluate the relative importance of the two different mechanisms for the formation of a trunk.

Acknowledgments. This work was supported by RBSP-ECT funding provided by JHU/APL Contract No. 967399 under NASA's Prime Contract No. NAS5-01072. Work at UNH was also supported by NASA under grant number NNX13AE23G. Work at LANL was performed under the auspices of the United States Department of Energy. HOPE data used in this paper were downloaded from the Van Allen Probes ECT website at http://www.rbsp-ect.lanl.gov/rbsp_ect.php. Solar wind plasma/IMF data and the Kp and $Sym-H$ indices were obtained from the GSFC/SPDF OMNIWeb interface at <http://omniweb.gsfc.nasa.gov>. D. R. Weimer provided the Weimer96 model for the ion tracings. J.-C. Zhang thanks Richard Thorne, Mike Liemohn, and Noé Lugaz for helpful discussions.

428 **References**

- 429 Boyle, C. B., P. H. Reiff, and M. R. Hairston (1997), Empirical polar cap potentials, *J.*
430 *Geophys. Res.*, *102*, A1, doi:10.1029/96JA01742.
- 431 Burlaga, L., E. Sittler, F. Mariani, and R. Schwenn (1981), Magnetic Loop Behind an
432 Inter-Planetary Shock - Voyager, Helios, and Imp-8 Observations, *J. Geophys. Res.*, *86*,
433 Na8, doi:10.1029/Ja086ia08p06673.
- 434 Buzulukova, N., and V. Vovchenko (2008), Modeling of proton nose structures in the
435 inner magnetosphere with a self-consistent electric field model, *J. Atmos. Sol.-Terr.*
436 *Phys.*, *70*, 2-4, doi:10.1016/j.jastp.2007.08.028.
- 437 Buzulukova, N. Y., R. A. Kovrazhkin, A. L. Glazunov, J. A. Sauvaud, N. Y. Ganushkina,
438 and T. I. Pulkkinen (2003), Stationary nose structures of protons in the inner
439 magnetosphere: Observations by the ION instrument onboard the Interball-2 satellite and
440 modeling, *Cosmic Res., Engl. Transl.*, *41*, 1, doi:10.1023/A:1022343327565.
- 441 Buzulukova, N. Y., Y. I. Galperin, R. A. Kovrazhkin, A. L. Glazunov, G. A.
442 Vladimirova, H. Stenuit, J. A. Sauvaud, and D. C. Delcourt (2002), Two types of ion
443 spectral gaps in the quiet inner magnetosphere: Interball-2 observations and modeling,
444 *Ann. Geophys.*, *20*, 3, doi:10.5194/angeo-20-349-2002.
- 445 Daglis, I. A., R. M. Thorne, W. Baumjohann, and S. Orsini (1999), The terrestrial ring
446 current: Origin, formation, and decay, *Rev. Geophys.*, *37*, 4, doi:10.1029/1999RG900009.

447 Ebihara, Y., L. M. Kistler, and L. Eliasson (2008), Imaging cold ions in the plasma sheet
 448 from the Equator-S satellite, *Geophys. Res. Lett.*, **35**, L15103,
 449 doi:10.1029/2008GL034357.

450 Ebihara, Y., M. Yamauchi, H. Nilsson, R. Lundin, and M. Ejiri (2001), Wedge-like
 451 dispersion of sub-keV ions in the dayside magnetosphere: Particle simulation and Viking
 452 observation, *J. Geophys. Res.*, **106**, A12, doi:10.1029/2000JA000227.

453 Ebihara, Y., M. Ejiri, H. Nilsson, I. Sandahl, M. Grande, J. F. Fennell, J. L. Roeder, D. R.
 454 Weimer, and T. A. Fritz (2004), Multiple discrete-energy ion features in the inner
 455 magnetosphere: 9 February 1998, event, *Ann. Geophys.*, **22**, 4, doi:10.5194/angeo-22-
 456 1297-2004.

457 Ejiri, M. (1978), Trajectory traces of charged-particles in the magnetosphere, *J. Geophys.*
 458 *Res.*, **83**, A10, doi:10.1029/JA083iA10p04798.

459 Ejiri, M., R. A. Hoffman, and P. H. Smith (1980), Energetic particle penetrations into the
 460 inner magnetosphere, *J. Geophys. Res.*, **85**, A2, doi:10.1029/JA085iA02p00653.

461 Fennell, J. F., et al. (1998), Multiple discrete-energy ion features in the inner
 462 magnetosphere: Polar observations, in *Physics of Space Plasmas*, edited, p. 395, MIT
 463 Center for Theoretical Geo/Cosmo Plasma Physics, Cambridge, MA.

464 Fok, M. C., J. U. Kozyra, A. F. Nagy, and T. E. Cravens (1991), Lifetime of ring current
 465 particles due to coulomb collisions in the plasmasphere, *J. Geophys. Res.*, **96**, A5,
 466 doi:10.1029/90JA02620.

467 Funsten, H. O., et al. (2013), Helium, Oxygen, Proton, and Electron (HOPE) Mass
 468 Spectrometer for the Radiation Belt Storm Probes Mission, *Space Sci. Rev.*,
 469 doi:10.1007/s11214-013-9968-7.

470 Ganushkina, N. Y., T. I. Pulkkinen, V. F. Bashkurov, D. N. Baker, and X. L. Li (2001),
 471 Formation of intense nose structures, *Geophys. Res. Lett.*, 28, 3,
 472 doi:10.1029/2000GL011955.

473 Gkioulidou, M., A. Y. Ukhorskiy, D. G. Mitchell, T. Sotirelis, B. H. Mauk, and L. J.
 474 Lanzerotti (2014), The role of small-scale ion injections in the buildup of Earth's ring
 475 current pressure: Van Allen Probes observations of the 17 March 2013 storm, *J. Geophys.*
 476 *Res.*, 119, 9, doi:10.1002/2014JA020096.

477 Goldstein, J., P. Valek, D. J. McComas, and J. Redfern (2012), TWINS energetic neutral
 478 atom observations of local-time-dependent ring current anisotropy, *J. Geophys. Res.*, 117,
 479 A11213, doi:10.1029/2012JA017804.

480 Gonzalez, W. D., J. A. Joselyn, Y. Kamide, H. W. Kroehl, G. Rostoker, B. T. Tsurutani,
 481 and V. M. Vasyliunas (1994), What is a geomagnetic storm?, *J. Geophys. Res.*, 99, A4,
 482 doi:10.1029/93JA02867.

483 Hodges, R. R. (1994), Monte carlo simulation of the terrestrial hydrogen exosphere, *J.*
 484 *Geophys. Res.*, 99, A12, doi:10.1029/94JA02183.

485 Jordanova, V. K., L. M. Kistler, J. U. Kozyra, G. V. Khazanov, and A. F. Nagy (1996),
 486 Collisional losses of ring current ions, *J. Geophys. Res.*, 101, A1,
 487 doi:10.1029/95JA02000.

488 Kessel, R. L., N. J. Fox, and N. Weiss (2013), The Radiation Belt Storm Probes (RBSP)
 489 and Space Weather, *Space Sci. Rev.*, doi:10.1007/s11214-012-9953-6.

490 Kistler, L. M., F. M. Ipavich, D. C. Hamilton, G. Gloeckler, B. Wilken, G. Kremser, and
 491 W. Studemann (1989), Energy-spectra of the major ion species in the ring current during
 492 geomagnetic storms, *J. Geophys. Res.*, *94*, A4, doi:10.1029/Ja094ia04p03579.

493 Kovrazhkin, R. A., J. A. Sauvaud, and D. C. Delcourt (1999), INTERBALL-Auroral
 494 observations of 0.1-12 keV ion gaps in the diffuse auroral zone, *Ann. Geophys.*, *17*, 6,
 495 doi:10.1007/S005850050802.

496 Kozyra, J. U., M. C. Fok, E. R. Sanchez, D. S. Evans, D. C. Hamilton, and A. F. Nagy
 497 (1998), The role of precipitation losses in producing the rapid early recovery phase of the
 498 Great Magnetic Storm of February 1986, *J. Geophys. Res.*, *103*, A4,
 499 doi:10.1029/97JA03330.

500 Lennartsson, W., E. G. Shelley, R. D. Sharp, R. G. Johnson, and H. Balsiger (1979),
 501 Some initial ISEE - 1 results on the ring current composition and dynamics during the
 502 magnetic storm of December 11, 1977, *Geophys. Res. Lett.*, *6*, 6,
 503 doi:10.1029/GL006i006p00483.

504 Li, X. L., D. N. Baker, M. Temerin, W. K. Peterson, and J. F. Fennell (2000), Multiple
 505 discrete-energy ion features in the inner magnetosphere: Observations and simulations,
 506 *Geophys. Res. Lett.*, *27*, 10, doi:10.1029/1999GL010745.

507 Liemohn, M. W., J. U. Kozyra, C. R. Clauer, and A. J. Ridley (2001), Computational
 508 analysis of the near-Earth magnetospheric current system during two-phase decay storms,
 509 *J. Geophys. Res.*, *106*, A12, doi:10.1029/2001JA000045.

510 Liemohn, M. W., J. U. Kozyra, V. K. Jordanova, G. V. Khazanov, M. F. Thomsen, and
 511 T. E. Cayton (1999), Analysis of early phase ring current recovery mechanisms during
 512 geomagnetic storms, *Geophys. Res. Lett.*, *26*, 18, doi:10.1029/1999GL900611.

513 Mauk, B. H., N. J. Fox, S. G. Kanekal, R. L. Kessel, D. G. Sibeck, and A. Ukhorskiy
 514 (2013), Science Objectives and Rationale for the Radiation Belt Storm Probes Mission,
 515 *Space Sci. Rev.*, doi:10.1007/s11214-012-9908-y.

516 Papitashvili, N. E., and J. H. King (2006), A draft high resolution OMNI data set, *EOS*
 517 *Trans. AGU, Jt. Assem. Suppl.*, *Abstract SM33A-02*, 87, 36.

518 Peterson, W. K., K. J. Trattner, O. W. Lennartsson, H. L. Collin, T. I. Pulkkinen, P. K.
 519 Toivanen, J. F. Fennell, J. L. Roeder, D. N. Baker, and T. A. Fritz (1998), Imaging the
 520 plasma sheet with energetic ions from the Polar satellite, in *Proc. of ICS-4*, edited, p. 813,
 521 Terra Sci. Publishing, Tokyo.

522 Ruffenach, A., et al. (2012), Multispacecraft observation of magnetic cloud erosion by
 523 magnetic reconnection during propagation, *J. Geophys. Res.*, *117*, A09101,
 524 doi:10.1029/2012JA017624.

525 Sergeev, V. A., and W. Lennartsson (1988), Plasma sheet at $X \approx -20$ RE during steady
 526 magnetospheric convection, *Planet. Space Sci.*, *36*, 4, doi:10.1016/0032-0633(88)90124-
 527 9.

528 Shirai, H., K. Maezawa, M. Fujimoto, T. Mukai, Y. Saito, and N. Kaya (1997),
 529 Monoenergetic ion drop-off in the inner magnetosphere, *J. Geophys. Res.*, *102*, A9,
 530 doi:10.1029/97JA01150.

531 Siscoe, G. L., G. M. Erickson, B. U. O. Sonnerup, N. C. Maynard, J. A. Schoendorf, K.
 532 D. Siebert, D. R. Wiemer, W. White, and G. R. Wilson (2002), Hill model of transpolar
 533 potential saturation: Comparisons with MHD simulations, *J. Geophys. Res.*, *107*(A6),
 534 1075, doi:10.1029/2001JA000109.

535 Smith, P. H., and R. A. Hoffman (1974), Direct observations in the dusk hours of the
 536 characteristics of the storm time ring current particles during the beginning of magnetic
 537 storms, *J. Geophys. Res.*, *79*, 7, doi:10.1029/JA079i007p00966.

538 Smith, P. H., and N. K. Bewtra (1978a), Charge exchange lifetimes for ring current ions,
 539 *Space Sci. Rev.*, *22*, 3.

540 Smith, P. H., and N. K. Bewtra (1978b), Charge-exchange lifetimes for ring current ions,
 541 *Space Sci. Rev.*, *22*, 3.

542 Spence, H. E., et al. (2013), Science goals and overview of the Radiation Belt Storm
 543 Probes (RBSP) Energetic Particle, Composition, and Thermal Plasma (ECT) Suite on
 544 NASA's Van Allen Probes Mission, *Space Sci. Rev.*, doi:10.1007/s11214-013-0007-5.

545 Tsyganenko, N. A., and M. I. Sitnov (2005), Modeling the dynamics of the inner
 546 magnetosphere during strong geomagnetic storms, *J. Geophys. Res.*, *110*, A03208,
 547 doi:10.1029/2004JA010798.

548 Vallat, C., N. Ganushkina, I. Dandouras, C. P. Escoubet, M. G. G. T. Taylor, H. Laakso,
 549 A. Masson, J. A. Sauvaud, H. Reme, and P. Daly (2007), Ion multi-nose structures
 550 observed by Cluster in the inner magnetosphere, *Ann. Geophys.*, *25*, 1,
 551 doi:10.5194/angeo-25-171-2007.

552 Weimer, D. R. (1996), A flexible, IMF dependent model of high-latitude electric
 553 potentials having "space weather" applications, *Geophys. Res. Lett.*, *23*, 18,
 554 doi:10.1029/96GL02255.

555 Weimer, D. R., and J. H. King (2008), Improved calculations of interplanetary magnetic
 556 field phase front angles and propagation time delays, *J. Geophys. Res.*, *113*, A01105,
 557 doi:10.1029/2007JA012452.

558 Weimer, D. R., D. M. Ober, N. C. Maynard, M. R. Collier, D. J. McComas, N. F. Ness,
 559 C. W. Smith, and J. Watermann (2003), Predicting interplanetary magnetic field (IMF)
 560 propagation delay times using the minimum variance technique, *J. Geophys. Res.*,
 561 *108(A1)*, 1026, doi:10.1029/2002JA009405.

562 Yamauchi, M., et al. (2006), Source location of the wedge-like dispersed ring current in
 563 the morning sector during a substorm, *J. Geophys. Res.*, *111*, A11s09,
 564 doi:10.1029/2006JA011621.

565 Yang, J., R. A. Wolf, F. R. Toffoletto, S. Sazykin, and C. P. Wang (2014), RCM-E
 566 simulation of bimodal transport in the plasma sheet, *Geophys. Res. Lett.*, *41*, 6,
 567 doi:10.1002/2014GL059400.

Zhang, J.-C., R. A. Wolf, S. Sazykin, and F. R. Toffoletto (2008), Injection of a bubble into the inner magnetosphere, *Geophys. Res. Lett.*, 35, L02110, doi:10.1029/2007GL032048.

Zhang, J.-C., M. W. Liemohn, J. U. Kozyra, B. J. Lynch, and T. H. Zurbuchen (2004), A statistical study of the geoeffectiveness of magnetic clouds during high solar activity years, *J. Geophys. Res.*, 109, A09101, doi:10.1029/2004JA010410.

Zhang, J.-C., R. A. Wolf, R. W. Spiro, G. M. Erickson, S. Sazykin, F. R. Toffoletto, and J. Yang (2009), Rice Convection Model simulation of the substorm-associated injection of an observed plasma bubble into the inner magnetosphere: 2. Simulation results, *J. Geophys. Res.*, 114, A08219, doi:10.1029/2009JA014131.

591 **Table 1. Properties of the Heavy Ion Trunk Structures**

UT	He ⁺ E (keV)	O ⁺ E (keV)	L	MLT	MLAT (°)
1627:20	3.5	4.5	3.6	9.1	-2.4
1653:20	1	2.5	2.8	10.0	-0.7
1659:00	0.1	1.8	2.7	10.4	-0.04
1700:40	0.04	1.5	2.6	10.5	0.09
1703:40	-	0.7	2.5	10.7	0.4

592

593

594

595

596

597

598

599

600

601

602

603

604

605

606

607

608

609

610

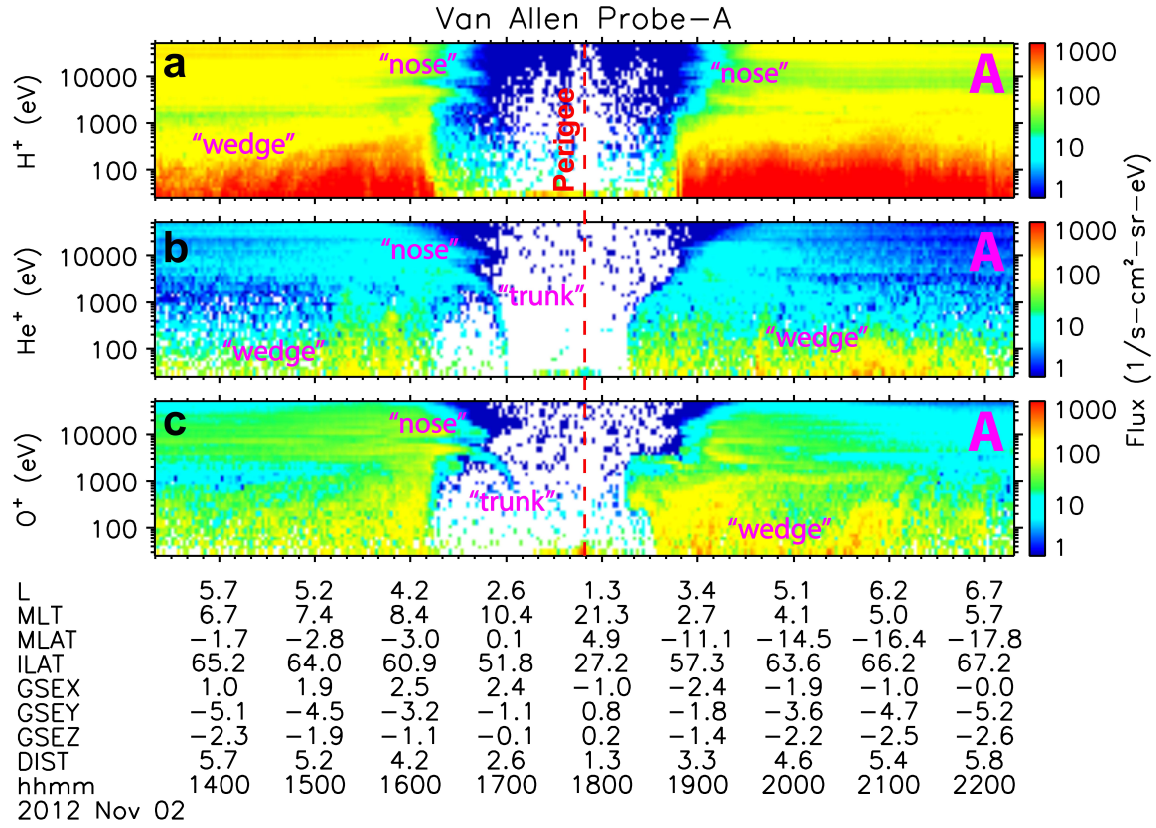


Figure 1. RBSP-ECT HOPE H^+ , He^+ , and O^+ spectrograms on the Van Allen Probe-A during an entire orbit, centered at perigee, on 2 November 2012. At the bottom is the ephemeris information of the Van Allen Probe: L (= L_{TS04}), magnetic local time (MLT, hours), magnetic latitude (MLAT, degrees), invariant latitude (ILAT, degrees), X, Y, and Z (R_E) in the GSE coordinate system, distance from the center of the Earth (DIST, R_E), and universal time (UT, hours). In each panel, the vertical red dashed line denotes the time of the perigee.

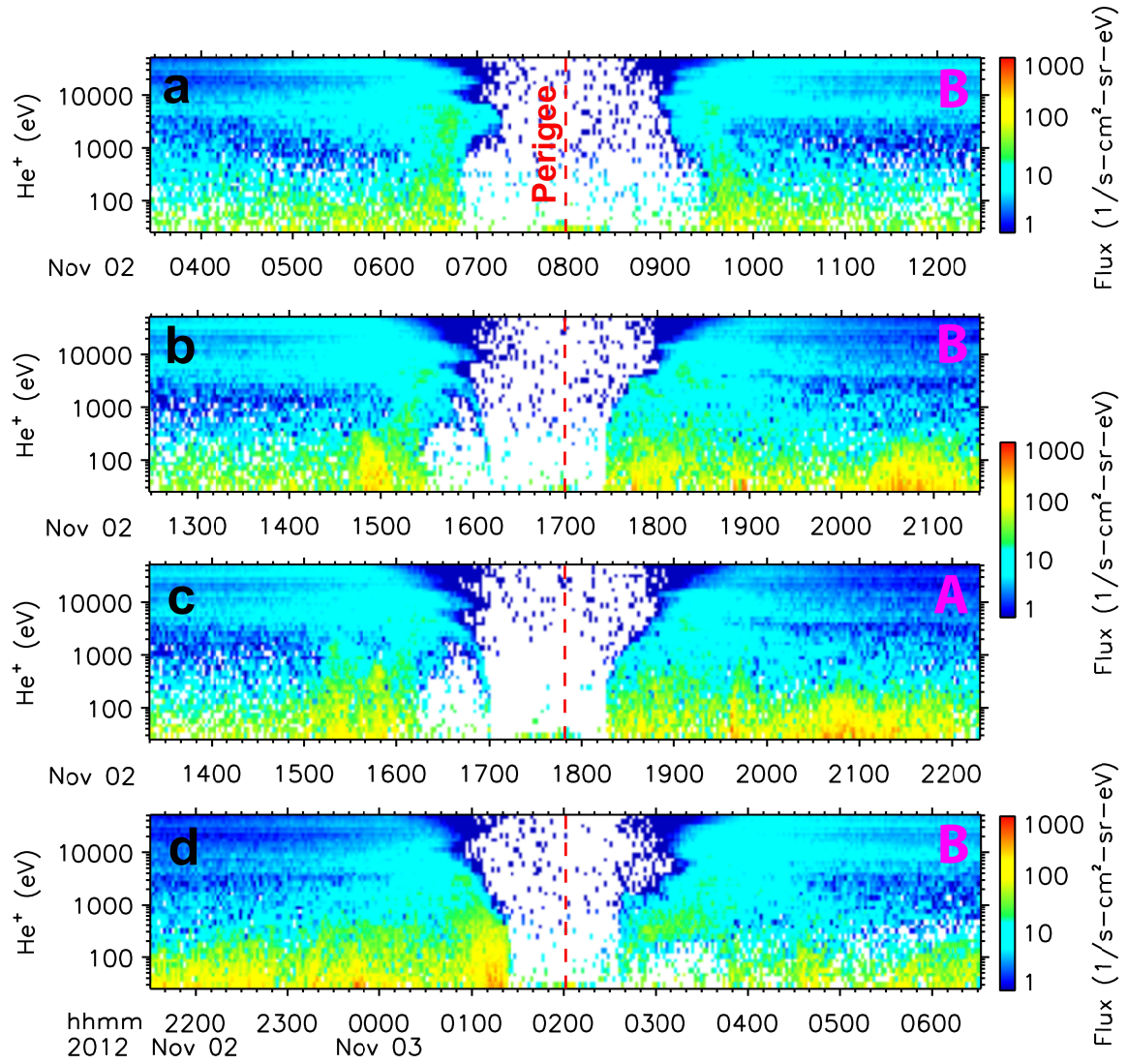


Figure 2. Similar format to Figure 1, but only for HOPE He^+ spectrograms on three consecutive orbits of the Van Allen Probe-B (a, b, and d) and one orbit of the Van Allen Probe-A (c). Panel c is identical to Figure 1b.

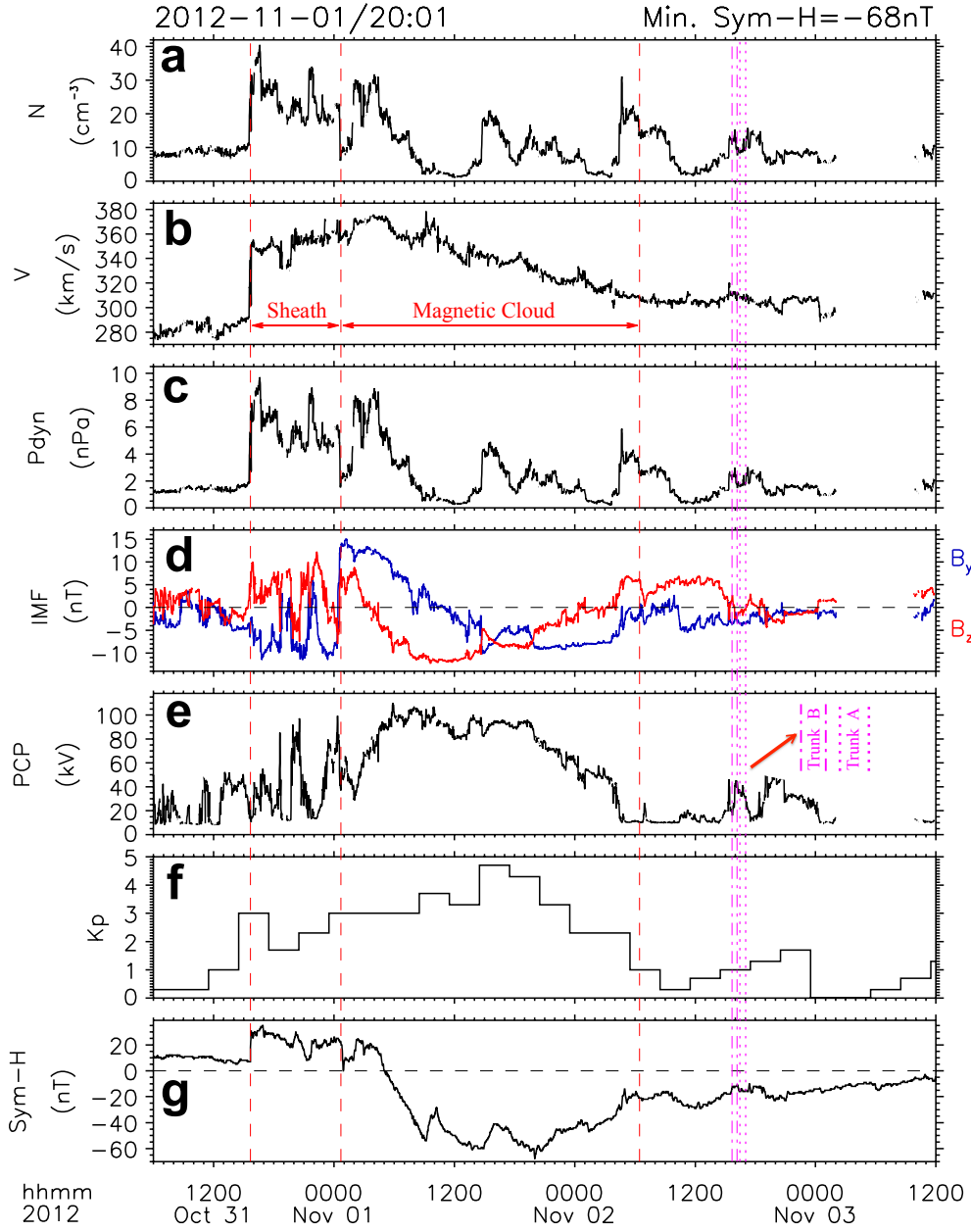


Figure 3. Solar wind plasma and interplanetary magnetic field (IMF) parameters, polar cap potential drop (PCP), K_p , and Sym-H from 0600 UT, 31 October to 1200 UT, 3 November 2012.

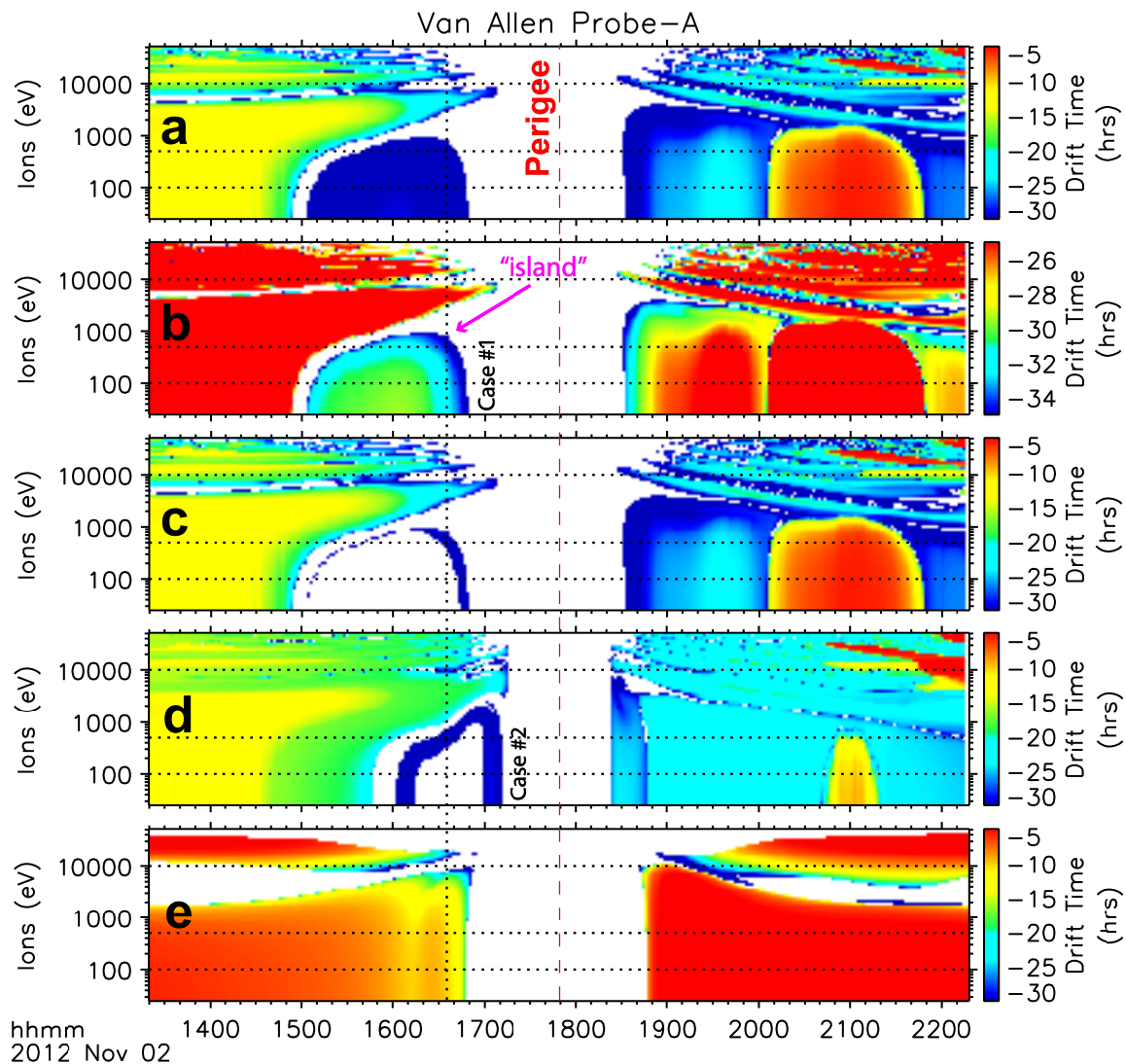


Figure 4. Calculated total ion backward drift time (negative) from the positions of the Van Allen Probe-A to the assumed ion source at $L = 10$ under different conditions: nominal tracing results with the color scale adjusted for two levels (a and b), assuming an ion source gap (c), under made-up “extreme” solar wind conditions (d), and using constant model inputs (e). The plotting time period is the same as that in Figure 1. The vertical red dashed line denotes the time of the perigee, the vertical black dotted line indicates the time of 1635 UT, and the horizontal dotted lines mark the energy values of 0.1, 0.5, and 10 keV.

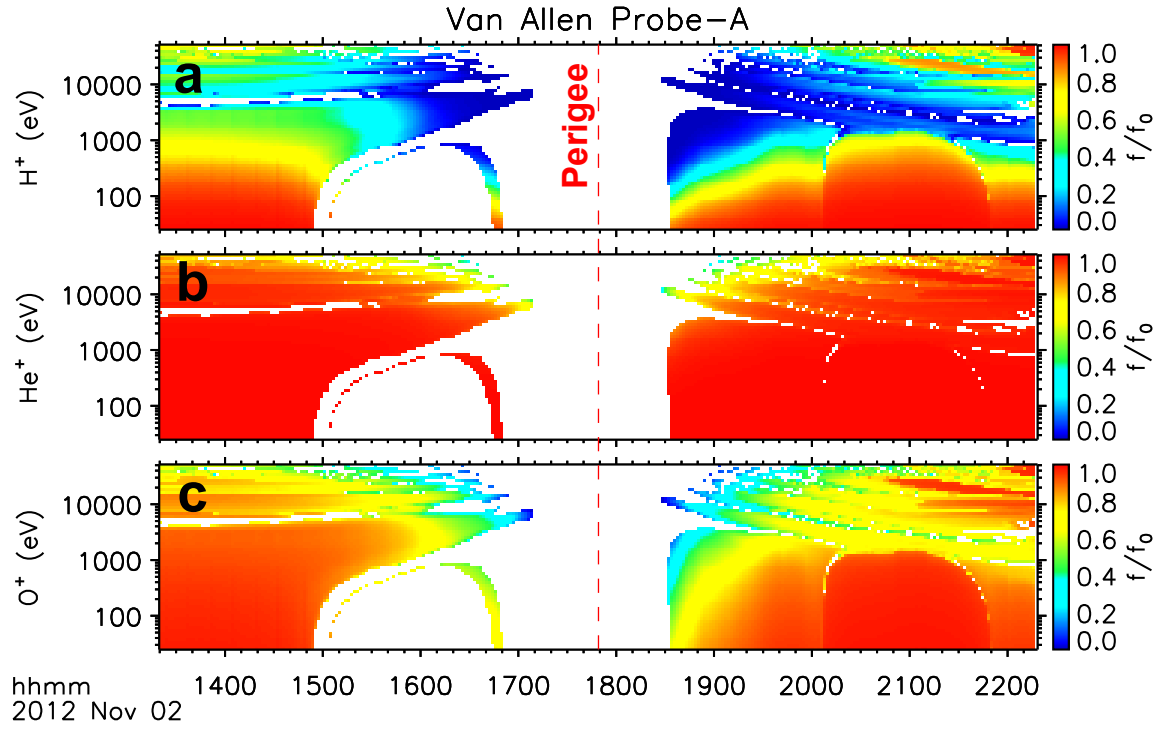


Figure 5. Calculated ratios of H^+ (a), He^+ (b), and O^+ (c) fluxes at the locations of the Van Allen Probe-A and in the assumed ion source at $L = 10$. The plotting time period is the same as Figure 1. The vertical red dashed line denotes the time of the perigee.

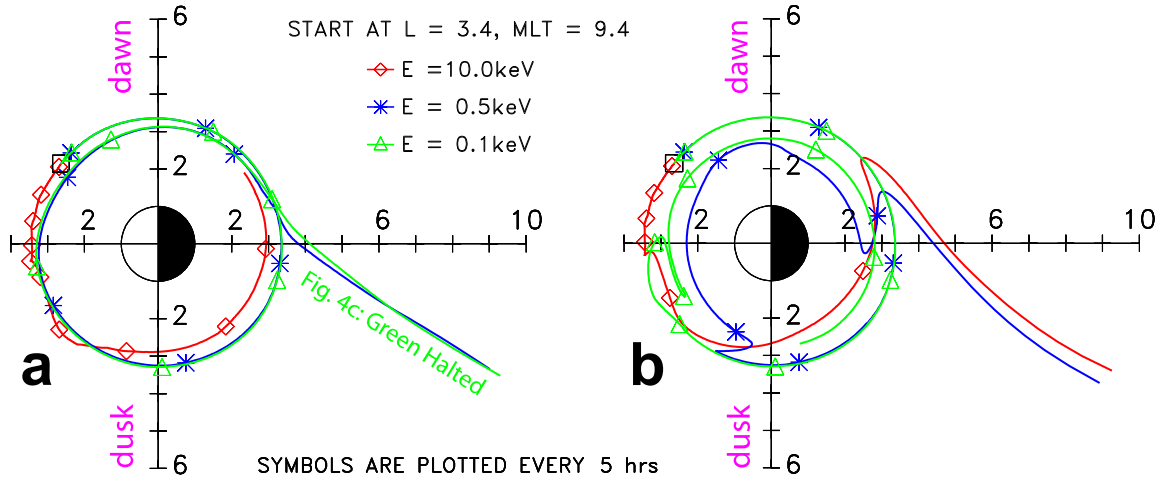
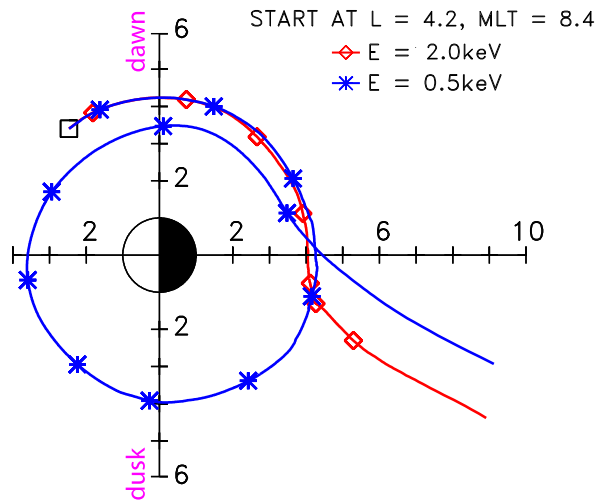


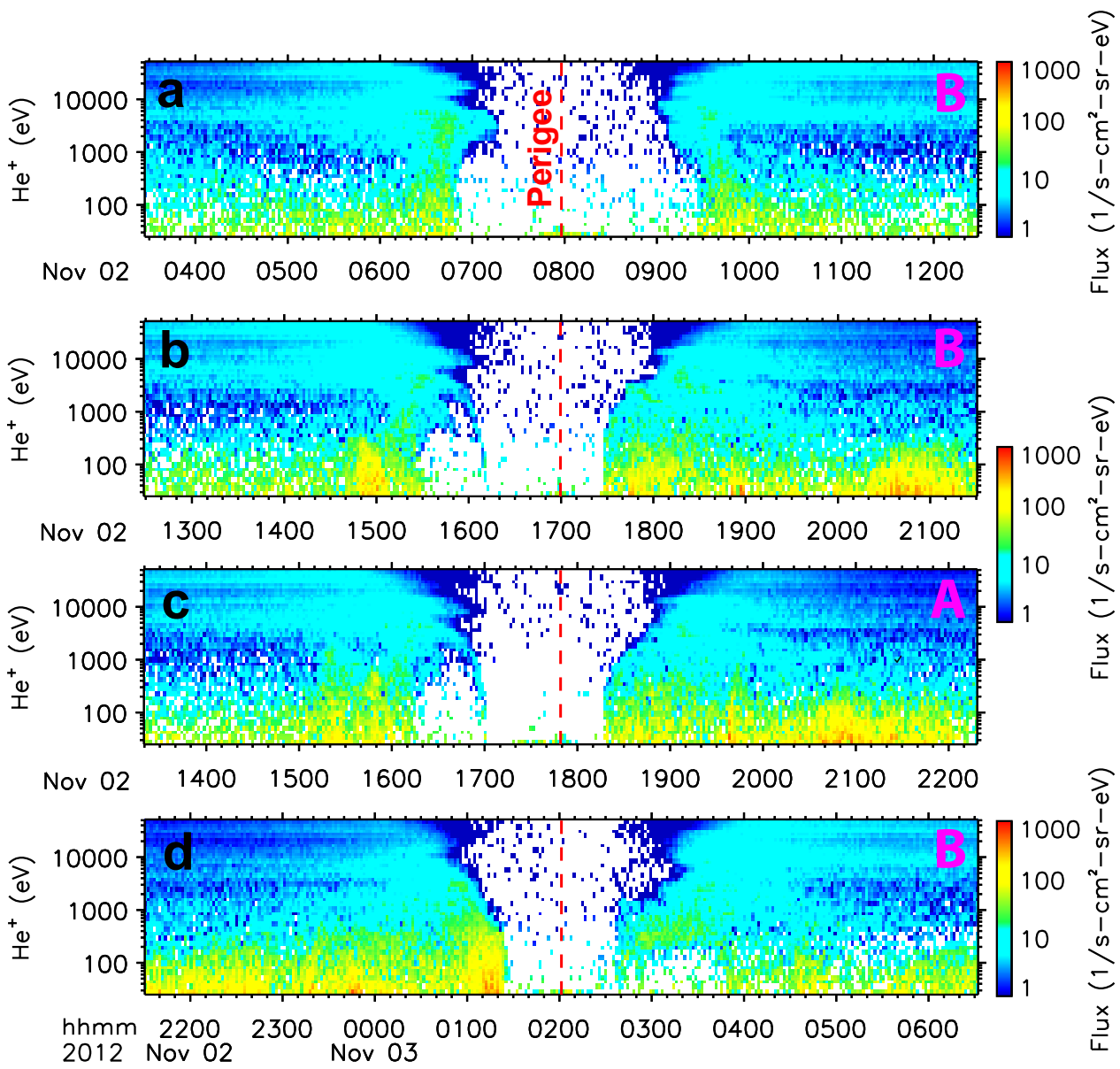
Figure 6. Fifty-hour backward tracing of drift paths for singly-charged ions ($PA = 90^\circ$) at 1635 UT, 2 November 2012, corresponding to the cases indicated in Figures 4b (a, left) and 4d (b, right). All backward drifting ions start from the position of the Van Allen Probe-A at the time point, i.e., from $L = 3.4$ and $MLT = 9.4$. The solid tracing trajectories are plotted every 30 seconds unless they reach the model boundaries at $L = 10$. The symbols, i.e., red squares, blue stars, or green triangles, are plotted every 5 hours until $L = 10$.

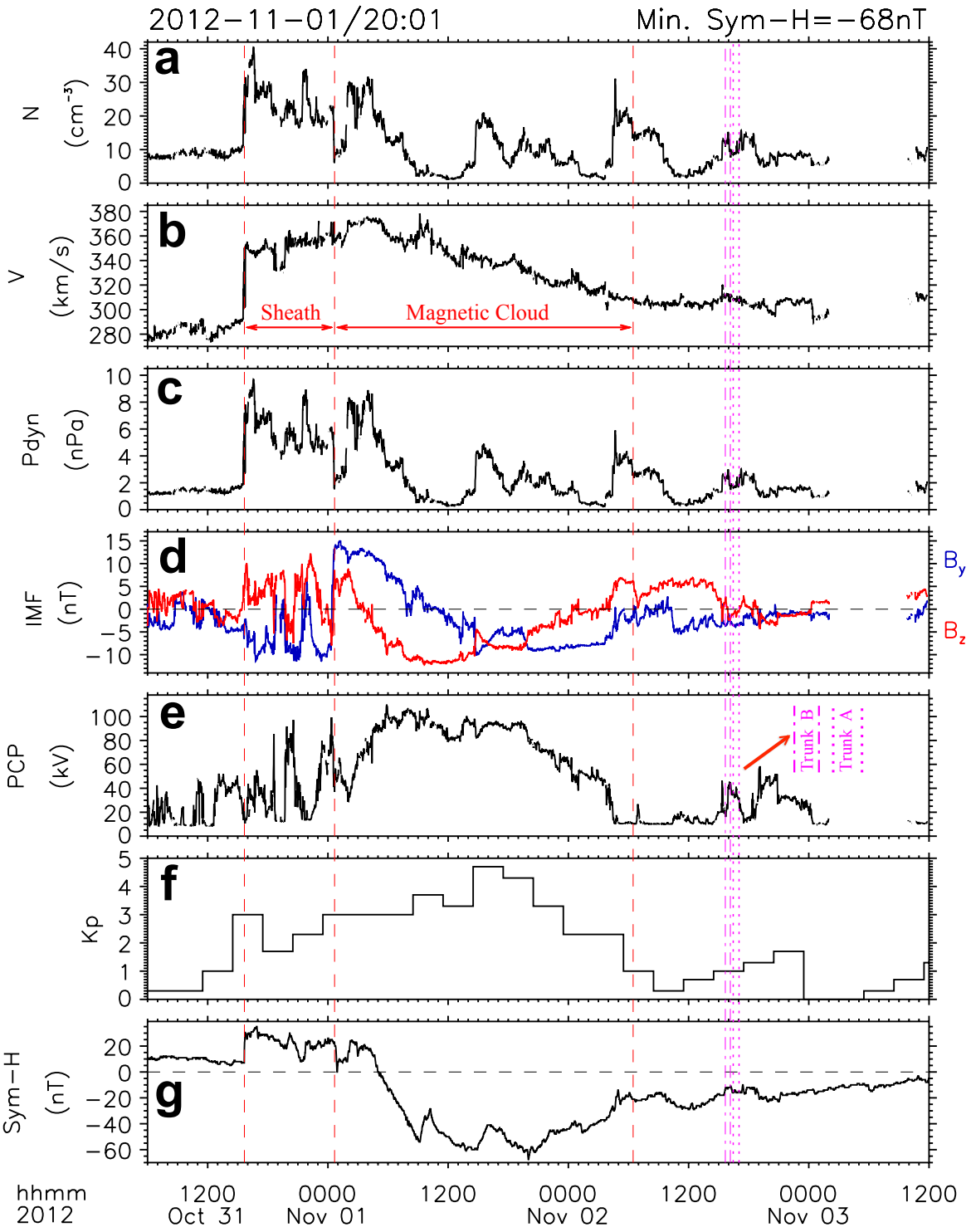


658

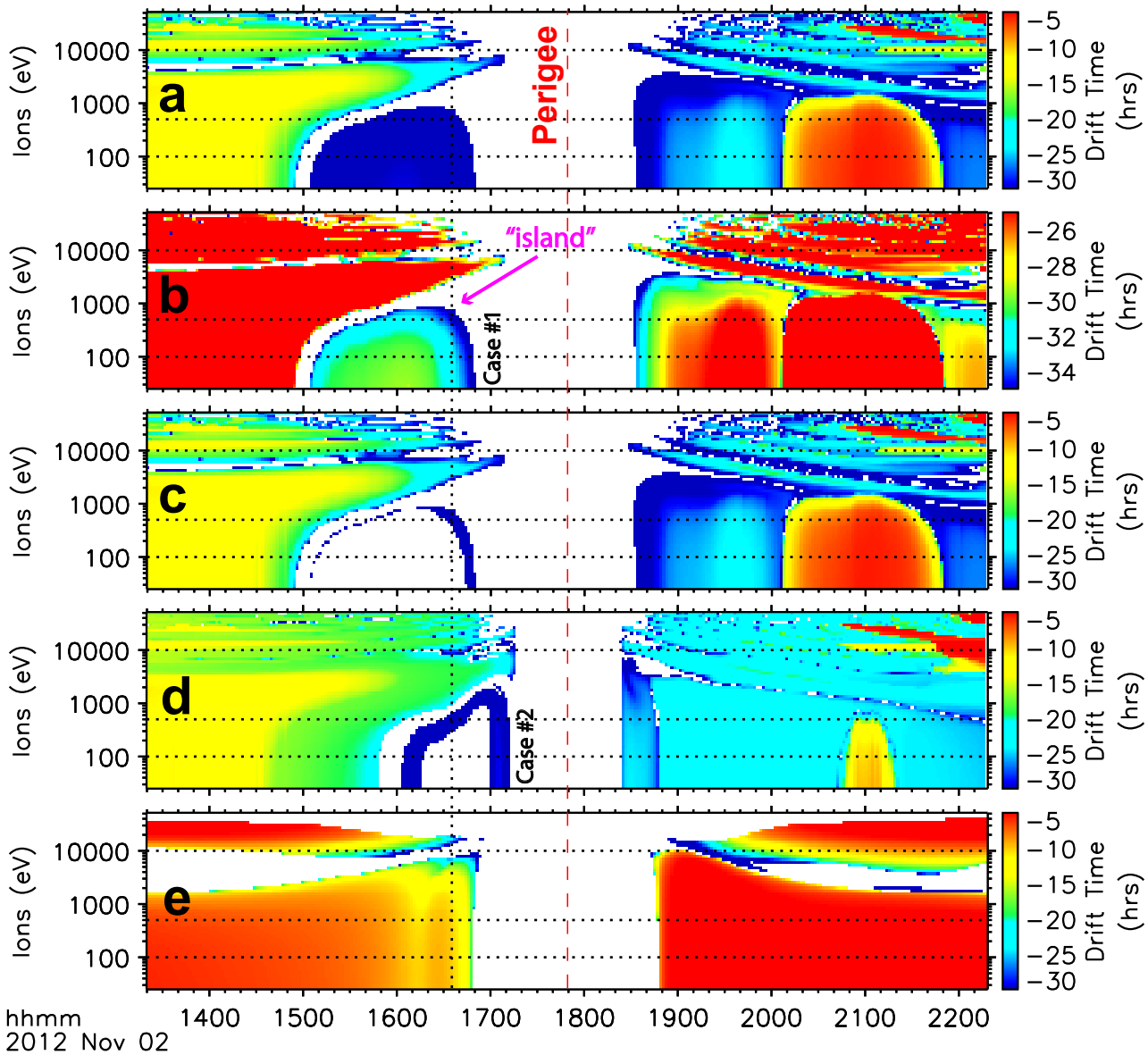
SYMBOLS ARE PLOTTED EVERY 3 hrs

659 **Figure 7.** Similar to Figure 6a, but for 0.5 and 2.0 keV singly-charged ions at 1600 UT,
 660 2 November 2012, starting from $L = 4.2$ and $MLT = 8.4$. The trajectory symbols are
 661 plotted every 3 hours until $L = 10$.

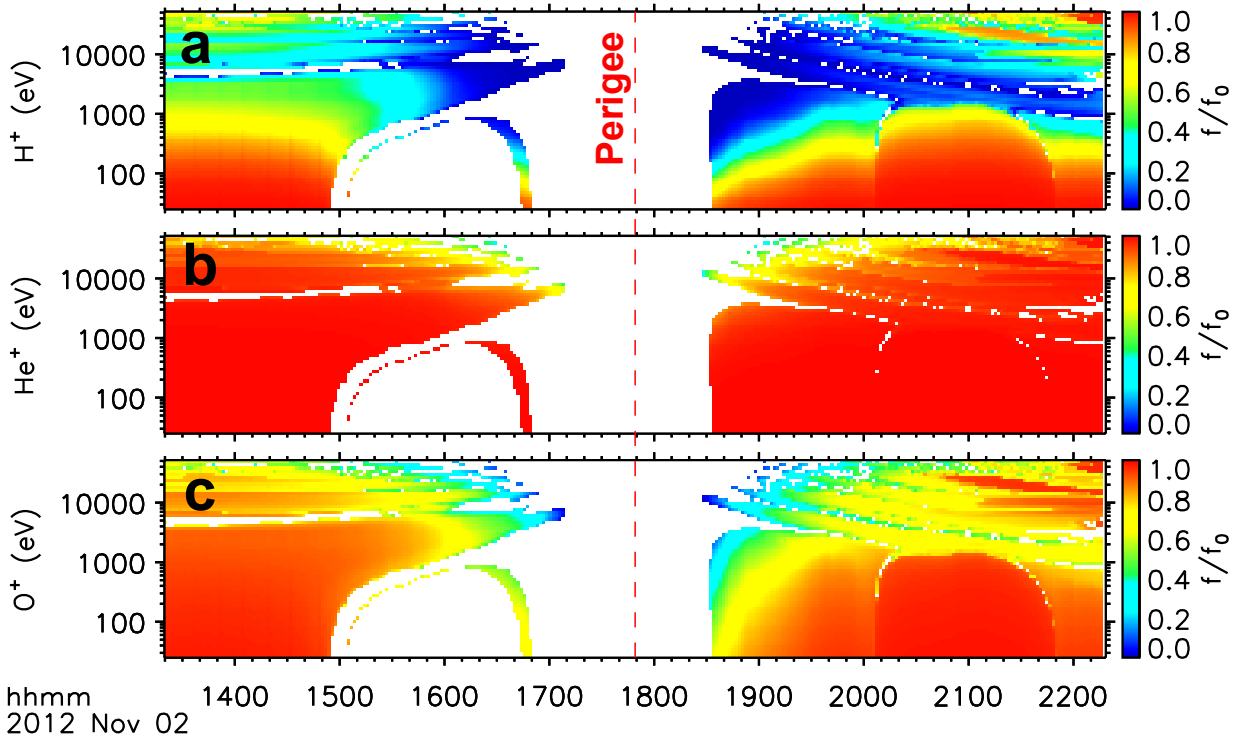


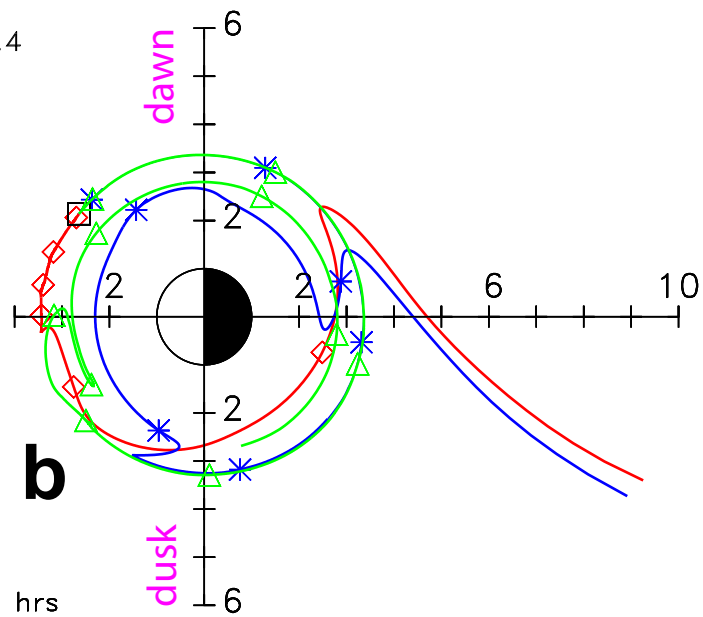
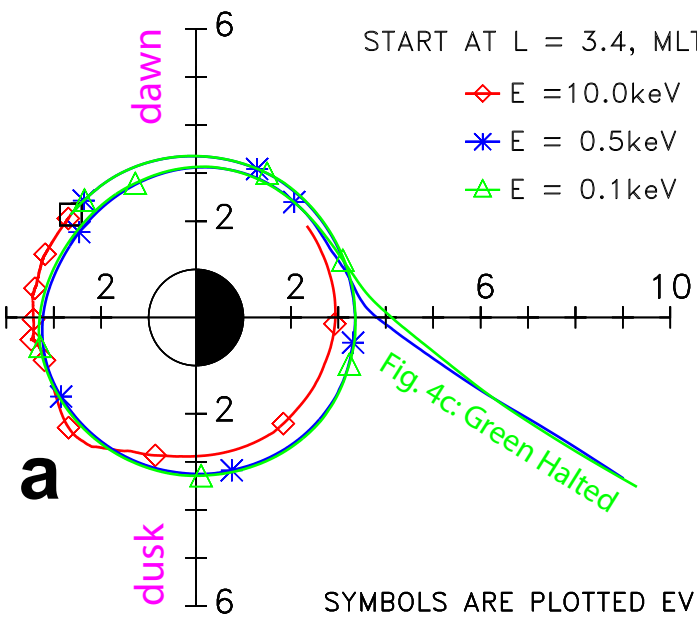


Van Allen Probe-A



Van Allen Probe-A

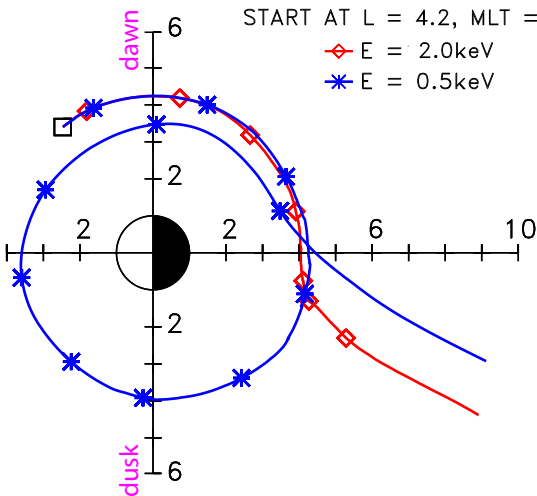




START AT L = 4.2, MLT = 8.4

◇ E = 2.0keV

* E = 0.5keV



SYMBOLS ARE PLOTTED EVERY 3 hrs